RESEARCH ARTICLE

NANO · MICRO small
www.small-journal.com

Ultrasensitive Raman Detection of Biomolecular Conformation at the Attomole Scale using Chiral Nanophotonics

Shailendra K. Chaubey, Rahul Kumar, Paula L. Lalaguna, Martin Kartau, Simona Bianco, Victor Tabouillot, Andrew R Thomson, Andrew Sutherland, Oleksiy Lyutakov, Nikolaj Gadegaard, Affar S. Karimullah, and Malcolm Kadodwala**

Understanding the function of a biomolecule hinges on its 3D conformation or secondary structure. Chirally sensitive, optically active techniques based on the differential absorption of UV–vis circularly polarized light excel at rapid characterisation of secondary structures. However, Raman spectroscopy, a powerful method for determining the structure of simple molecules, has limited capacity for structural analysis of biomolecules because of intrinsically weak optical activity, necessitating millimolar (mM) sample quantities. A breakthrough is presented for utilising Raman spectroscopy in ultrasensitive biomolecular conformation detection, surpassing conventional Raman optical activity by 15 orders of magnitude. This strategy combines chiral plasmonic metasurfaces with achiral molecular Raman reporters and enables the detection of different conformations (α-helix and random coil) of a model peptide (poly-L/D-lysine) at the ≤attomole level (monolayer). This exceptional sensitivity stems from the ability to detect local, molecular-scale changes in the electromagnetic (EM) environment of a chiral nanocavity induced by the presence of biomolecules using molecular Raman reporters. Further signal enhancement is achieved by incorporating achiral Au nanoparticles. The introduction of the nanoparticles creates highly localized regions of extreme optical chirality. This approach, which exploits Raman, a generic phenomenon, paves the way for next-generation technologies for the ultrasensitive detection of diverse biomolecular structures.

1. Introduction

Delineating the dynamic 3D structures and associated conformational transitions of biomolecules is of paramount importance in biophysics and life sciences. These intricate conformational shifts underpin the diverse biological functions of biomolecules, from the exquisite selectivity of enzyme catalysis to the intricate signalling cascades within cells. While chirally sensitive spectroscopic methods are established workhorses for rapid biomolecular structure characterisation, their inherent sensitivity limitations (~μM range) pose a significant challenge. This limitation severely hinders their applicability in crucial areas demanding ≤femtomolar (fM) detection sensitivity. For instance, analysing the ultra-low concentrations of chiral metabolites and drugs within biofluid (blood, mucus, etc) necessitates enhanced sensitivity to probe their intricate conformational landscapes.

Nanophotonic platforms have emerged as promising tools to overcome these

S. K. Chaubey, R. Kumar, P. L. Lalaguna, M. Kartau, S. Bianco, V. Tabouillot, A. R Thomson, A. Sutherland, A. S. Karimullah, M. Kadodwala
School of Chemistry
Joseph Black Building
University of Glasgow
Glasgow G12 8QQ, UK
E-mail: shailendrakumar.chaubey@glasgow.ac.in; malcolm.kadodwala@glasgow.ac.uk

O. Lyutakov
Department of Solid-State Engineering
University of Chemistry and Technology
Prague 16628, Czech Republic

N. Gadegaard
James Watt School of Engineering
Rankine Building
University of Glasgow
Glasgow G12 8QQ, UK

The ORCID identification number(s) for the author(s) of this article can be found under https://doi.org/10.1002/smll.202404536

DOI: 10.1002/smll.202404536

sensitivity limitations in chiral detection.[1–5] These platforms capitalise on monitoring perturbations in the local electromagnetic (EM) environment induced by the presence of chiral molecules, offering a significant departure from the weak dichroic phenomena employed in traditional methods. This approach enables the utilisation of plasmonic nanostructures, leading to enhanced sensitivity and greater flexibility compared with conventional techniques. However, current nanophotonic platforms face challenges due to highly localized EM field changes. These limitations restrict the observed far-field optical response asymmetries, which are crucial for detection, and consequently favour larger biomolecules with a significant near-field footprint (≥10 kDa). This significantly hinders the investigation of smaller molecules like polypeptides, which play vital roles in cellular processes and drug development and whose conformational dynamics are equally critical to elucidate.

Here, we introduce a novel paradigm for chiral spectroscopy capable of probing the conformational structures of small biomolecules at the attomole level. We demonstrate the discrimination between the random coil and α-helical conformations of the model polypeptide poly-L-/D-lysine (PL) beyond the attomole limit. This approach leverages nonchiral reporter molecules to detect changes induced in the EM environment near the target molecule. The level of perturbation correlates with the conformational structure, mimicking the principle behind conventional circular dichroism (CD)-based techniques for secondary structure differentiation. We demonstrate that using a common achiral Raman reporter, biphenyl-4,4′-dithiol (BPDT), and monitoring EM environments at a molecular scale using enantiomeric metasurfaces composed of shuriken-shaped nanocavities, chirality-based conformational discrimination can be achieved at attomole levels. Co-deposition of Au nanoparticles enhances the BPDT signal intensity, improving signal-to-noise detection.

This novel approach offers a 15 orders of magnitude improvement in sensitivity compared with conventional chirally sensitive Raman optical activity (ROA).[6,7] Furthermore, it surpasses prior amplified nanophotonic Raman-based chirality detection approaches by 9 orders of magnitude.[4,8] These previous studies lacked conformational sensitivity and required micrometre-thick samples. Our proposed method has ideal traits for translation into analytical technologies. It utilises Raman scattering, a widely used tool in chemical sciences, and leverages chiral metasurfaces on polycarbonate templates, fabricated using high-throughput injection moulding, promising scalability and practical application.

2. Results and Discussion

2.1. Nanophotonic Platform

The chiral Au metasurfaces used in this study consisted of periodic square arrays of six-armed chiral "shuriken" shaped nanocavities, **Figure 1a**. The metasurfaces were formed by depositing 100-nm-thick Au films on nanopatterned polycarbonate templates, which have been described in detail elsewhere.[9–11] Similar Au metasurfaces have been used in chiral sensing applications in which far field extinction[11–17] and luminescence[17,18] spectra have been used to monitor asymmetries in EM environments. Reflection and optical rotation dispersion (ORD) spectra from enantiomorphic films were collected in air to display multiple resonances. As expected, similar reflection spectra were obtained from both enantiomorphs, which displayed a broader resonance in the 550–560 nm spectral range and another sharper resonance in 700–760 nm spectra, Figure 1d. Equal and opposite ORD spectra are obtained from the enantiomorphic pairs, and both have resonances in the 550–600 nm range with bisignate line shapes (See S1, Supporting Information).

BPDT was chosen for this study for two reasons: 1) it has a very large Raman scattering cross-section,[19–21] thus making it an effective reporter molecule; and 2) it has two thiol functional groups, enabling it to chemisorb to the metasurface and bind to the Au nano particle (NP).

2.2. Benchmarking Experiments with L-/D-/Racemic-Cysteine and L-Glutathione

Before pursuing a study of the more structurally complex polylysine systems, the veracity of the proposed concept was benchmarked against structurally simpler systems. In the first instance, self-assembled monolayers (SAM) of L-/D-/racemic-cysteine only, BPDT only, or mixed L-/D-/racemic-cysteine and BPDT were deposited from aqueous solutions onto the chiral metasurfaces. Both cysteines and BPDT formed chemisorbed moieties through the cleavage of the S—H bond and the formation of strong S—Au bonds.[22–24] Cysteine is expected to form a chemisorbed zwitterion on the surface.[22,23,25] An important question to address was whether the adsorbed cysteine and BPDT moieties were inter-mixed or phase-separated into individual domains. From the Raman microscopy maps obtained, metafilms with co-adsorbed cysteine and BPDT (See S2, Supporting Information) showed no evidence of the formation of separate domains of significant size. Reflectance spectra collected after the deposition of the mixed cysteine / BPDT, Figure 1d) and all other SAMs (See S3, Supporting Information) showed no significant shifts relative to those collected prior to functionalization. The adsorption of cysteine on a range of Au surfaces has been extensively studied using various techniques.

The accepted coverages of cysteine within known surface structures are of the order of $\approx 2.0 \times 10^{14}$ molecules cm^{-2}.[24,25] Thus, within the ≈ 100 μm^2 laser spot size sampled by Raman microscopy, there are $\leq 300 \times 10^{-18}$ moles (≤300 attomoles) of cysteine.

Au NPs of either 20 or 30 nm diameter were deposited on the cysteine/BPDT SAM functionalised metasurfaces. Scanning electron microscopy (SEM) images, Figure 1b,c, collected after deposition, show that the surface density of 20 nm is greater than that of 30 nm diameter NPs. In addition, 20 nm diameter NPs have a greater heterogeneity in spatial distribution than the larger-diameter NPs. The greater spatial heterogeneity displayed by the 20-nm NPs is attributed to the smaller diameter, which allows adsorption within the "arms" of the shuriken structure. In contrast, the 30-nm particles are comparable in size to the arm cavity. Both 20- and 30-nm NPs have a propensity to bind to the side wall of the nanocavity. This behaviour would be consistent with a thermodynamic driver to maximise the coordination of the NP to the free thiol groups of the BPDT because it

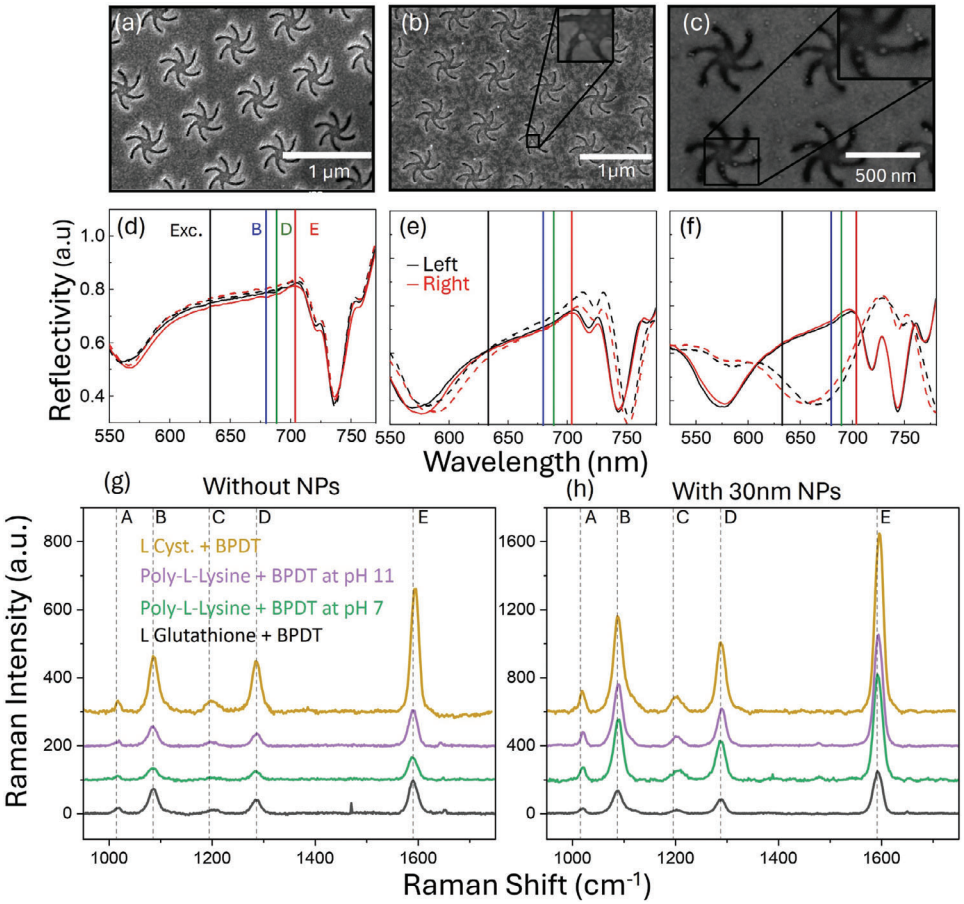

Figure 1. SEM images of LH metasurfaces: a) without nanoparticles; b) with 30-nm nanoparticles; and c) with 20-nm nanoparticles with a cysteine and BPDT molecular layer. Reflection spectra corresponding to (a), (b) and (c) collected before (solid) and after (dotted) deposition are shown in (d), (e), and (f). g,h) Raman Spectra from different samples showing their respective Raman intensities for comparison. Each spectrum is shifted vertically by 100 and 200 counts to aid comparison in the case of no NPs and 30 nm NPs, respectively. The black line in the reflection spectra shows the excitation wavelength, and the blue, green, and red lines correspond to the wavelengths of the three major Raman peaks labeled as B, D, and E in the Raman spectra.

allows the particle to bind both to the surfaces of the walls and bottom of the cavity simultaneously. Consequently, this results in 30 nm NP favouring binding sites in the regions at the entrance of the arm cavity. As expected, reflectance spectra collected after NPs deposition show significant red shifts in the plasmonic resonances, Figure 1e,f, with the largest shift observed for the 20-nm-diameter NPs.

In the presence and absence of NPs, there was no observable asymmetry in the reflection or ORD spectra collected from enantiomorphic metasurfaces that had been functionalised with SAMs containing L-or D-cysteine. Thus, no enantiomeric detection of cysteine is possible using extinction spectra-based measurements.

Collection of surface enhanced Raman scattering (SERS) spectra was attempted from all the SAM functionalised surfaces, both metasurface and for references unstructured Au, in the absence and presence of Au NP, Figure 1g. Each displayed spectrum is the average of spectra taken from three different arrays of the same enantiomorph, and each of these are the average of five different measurements. A SERS response was only observed from metasurfaces that had been functionalised with SAM-containing BPDTs. The observed SERS spectra are solely dominated by bands associated with BPDT, which is consistent with the much weaker Raman scattering cross-section of cysteine. The spectra obtained in this work are very similar to those obtained previously from BPDT immobilised on either Au nanoparticles or commercial SERS (Klarite) substrates.[26] The characteristic spectrum of BPDT has five dominant peaks, at 1020, 1084, 1200, 1285 and 1590 cm^{-1}, which are labelled A, B, C, D, and E, respectively. The

Table 1. Vibrational mode assignments and labelling of BPDT Raman spectra based on reference (18) are tabulated.

Raman peak position	Labeled as	Vibrational mode assigned
1020 cm^{-1}	A	Ring Deformation
1084 cm^{-1}	B	C_{ring} —S in plane
1200 cm^{-1}	C	12 C—H in plane
1285 cm^{-1}	D	Inter Ring C—C Stretching
1590 cm^{-1}	E	C—C Stretching

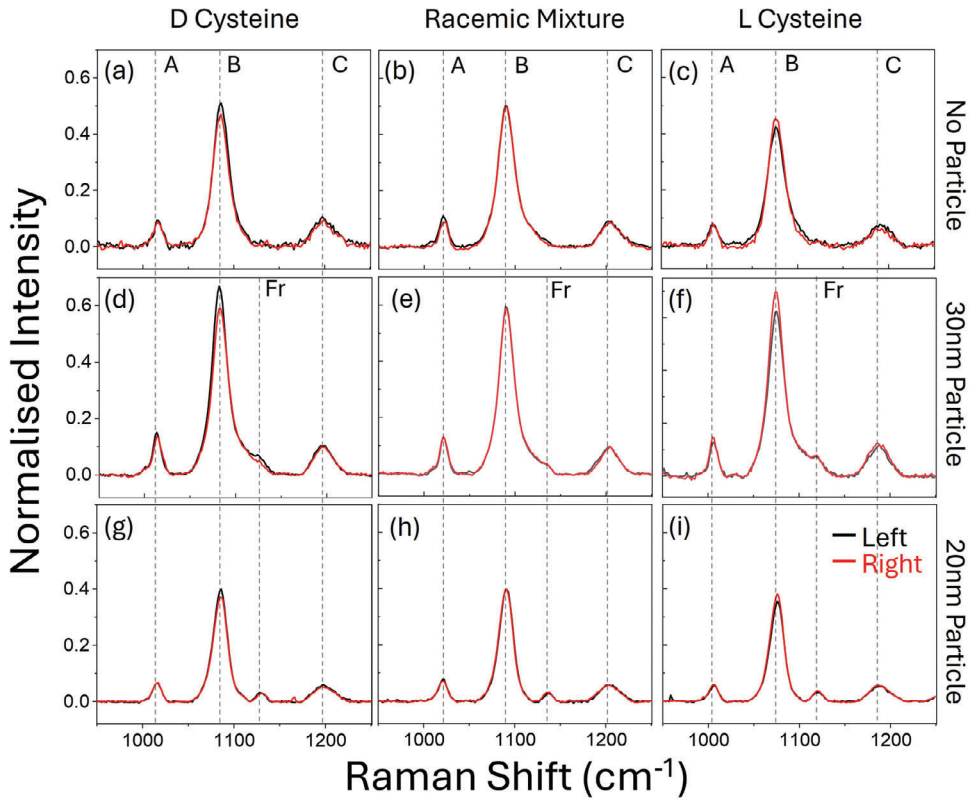

Figure 2. Raman spectra normalized at 1590 cm^{-1} collected from left (black) and right (red) metasurfaces spanning the A, B and C Raman peaks: a–c) only BPDT + Cysteine; d–f) with 30 nm NPs; and g–i) with 20 nm NPs.

vibrational assignments of these modes are given in **Table 1**. In the absence of NPs, the Raman response of mixed BPDT/cysteine layers were ≈30% of that of pure BPDT layers. This implies that the mixed SAMs contain ~70% cysteine. Adding 30 and 20 nm particles enhances the Raman signal significantly. An additional peak at 1130 cm^{-1} is visible in the Raman spectra of the NP-containing layers. A similar feature has been observed in previous studies involving Au NPs and has been attributed to Fermi resonance, labelled Fr in **Figures 2**, **3** and **6**.[20]

The introduction of the NPs enhances the BPDT Raman signals from the mixed layers, with the presence of 20 and 30 nm NPs increasing the response by ≈3.8 and 2.8 times, respectively.

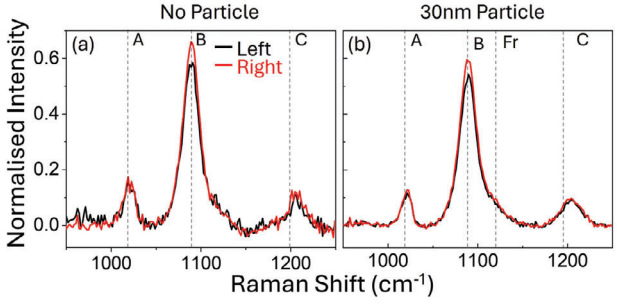

Figure 3. Raman spectra normalized at 1590 cm^{-1} collected from the left (black) and right (red) metasurfaces spanning the A, B, and C Raman peaks: a) L-Glutathione + BPDT; b) with 30 nm NPs.

Although the overall enhancement factors are similar, the much smaller concentration of the 30 nm NP makes them significantly more effective per particle.

To account for sample-to-sample variations in the absolute intensities of the Raman signal, and hence aid comparison, all spectra have been normalized to the peak E. Figures 2a–i and 3a,b show the normalized spectra in the case of cysteine and glutathione. These spectra clearly demonstrate asymmetric Raman responses from enantiomeric pairs of metasurfaces when adsorbed with L- or D-cysteine, and L-glutathione. Peak B showed significant intensity asymmetries between enantiomorphs, the sign of which depended on the handedness of the adsorbed cysteine and glutathione. In the absence of L-, D-cysteine or L-glutathione or for racemic cysteine, there is no asymmetry in the Raman response from the enantiomorphic pairs of metasurfaces (See S4, Supporting Information). In **Figure** 4a–d, difference spectra derived from the subtracting left minus right metasurface data. The shaded region in the difference spectra shows the standard deviation of 15 measurements collected from three samples. The greater Raman response generated by the introduction of the NP improved the signal-to-noise ratio of the difference spectra. However, only the 30 nm NPs result in an increase in the level of asymmetry, whereas the 20 nm NPs give a smaller asymmetry than that observed from just the mixed layers. For 20 nm particle standard deviation is larger and it can be attributed to the more heterogeneous spatial distribution of the NPs. Although the addition 30 nm Au nanoparticles to glutathione-containing layers increased the signal-to-noise ratio, no significant increase

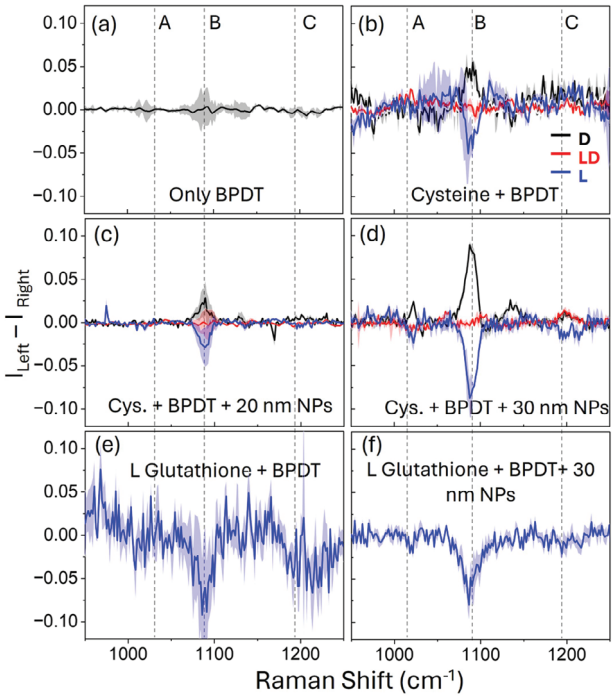

Figure 4. The difference spectra derived from the Raman intensities from left and right-handed chiral metasurfaces ($I_{left} - I_{right}$), for: a) BPDT only. b) BPDT mixed with L-D- and LD (racemic)- cysteine; c) BPDT with L-D- and LD (racemic)- cysteine and 20 nm NPs; d) BPDT with L-D- and LD (racemic)- cysteine and 30 nm NPs; e) BPDT with L-glutathione; (and f) BPDT with L-glutathione nm NPs. The shaded region in each spectrum represents the standard deviation derived from 15 measurements collected from three sets of arrays.

in asymmetry in the different spectra was observed, Figure 4e,f. The structural complexity of glutathione, which includes an additional asymmetric centre compared to cysteine, might influence its interaction with nanoparticles, leading to an improvement in signal-to-noise ratio but not in overall signal enhancement. This increased complexity could result in more variable interactions, explaining why the signal enhancement for glutathione is less pronounced. These distinctions highlight the differing impacts of molecular structure on the interaction with nanoparticles and their spectral responses.

2.3. Validating Experiments with Numerical EM Simulations

The central premise of this study is that the experimentally observed asymmetries in the Raman responses from enantiomorphic pairs are the result of asymmetric changes in the EM environments caused by the presence of single enantiomers of chiral molecules. To validate this hypothesis, numerical EM simulations were performed using the finite element method implemented on the COMSOL Multiphysics platform. Simulations were performed using an idealised model shuriken structure (see S5–S7, Supporting Information) and the chiral layer. The model consists of a "perfect" shuriken structure covered by a 5-nm dielectric layer (refractive index = 1.44) that can be assigned a Pasteur factor (ξ)to parameterise its chiroptical response. The equation used to calculate the electric field in the isotropic chiral medium:

$$D = \epsilon_0 \epsilon_r E + i\xi B \tag{1}$$

$$H = \frac{B}{\mu} + i\xi E \tag{2}$$

here ϵ_0 is the permittivity of free space, and ϵ_r is the relative permittivity. μ is the permeability. E is the complex electric field, B is the complex magnetic flux density, H is the magnetic field, and D is the electric displacement. ξ is the Pasteur factor which is nonzero for chiral dielectric and sign of this factor accounts for the handedness of the chiral dielectric. Its value can be estimated with a general formula.

$$\xi = \beta_c \left(\frac{1}{\hbar\omega + \hbar\omega_0 + i\Gamma_{12}} + \frac{1}{\hbar\omega - \hbar\omega_0 + i\Gamma_{12}} \right) \tag{3}$$

The parameters in equation (3) can be estimated from the quantum equation of motion of density matrix assuming a low density of molecules.[27,28] Here β_c is an intrinsic coefficient that determines the magnitude of chiral properties, and we use $\beta_c = 4.1 \times 10^{-4}$. Here $\hbar\omega_0$ (where $\hbar$ is the reduced Planck's constant $h/2\pi$ and ω_0 is the absorption frequency) and Γ are the energy and intrinsic width of the resonant chiral excitation of the dielectric. Consequently, the value of ξ at a particular wavelength is dependent on the chiroptical properties of the chiral dielectric.

A cysteine/glutathione monolayer would have a thickness of ≈ 0.5 nm, however, due to computational constraints, a greater thickness was required. This means that a smaller ξ should be used in the model than is physically realistic to offset the larger volume occupied by the chiral dielectrics. Further simplifications were made for the models that incorporate the NP. Only a single NP was included in these models at a single site, which based on the SEM images, Figure 1b,c is a reasonable assumption for a 30 nm particle, but unrealistic for the 20 nm particle. A midpoint in the arm cavity was the location of the 20-nm NP. For the 30-nm case, the NP was placed at the entrance of the arm cavity.

Estimates of the relative intensities of the Raman signal can be derived from the EM simulations using the volume-averaged magnitudes of the electric fields within the chiral layer of the models. The magnitude of the Raman response of a particular band (I_i) is:

$$I_i \propto |E_{ex}|^2 |E_i|^2 \tag{4}$$

where $|E_{ex}|$ and $|E_i|$ are the volume-averaged field magnitudes at the excitation (632.8 nm) and Raman band wavelengths, respectively. Consequently, the level of asymmetry (g) observed in the difference spectra was derived as follows:

$$g = \left(\frac{|E_L^{Ex}|^2 |E_L^B|^2}{|E_L^{Ex}|^2 |E_L^E|^2} - \frac{|E_R^{Ex}|^2 |E_R^B|^2}{|E_R^{Ex}|^2 |E_R^E|^2} \right) \tag{5}$$

where $|E_{L(R)}^{Ex}|$ are the magnitude of the electric fields at the excitation wavelength for the left (right) metasurfaces, while $|E_{L(R)}^{B(E)}|$ are the magnitude of the electric fields at the wavelength of the B (E) peak of the left (right) enantiomorphs. The asymmetries were

Table 2. Comparison of experimental asymmetries with those derived from numerical simulations for two ξ values.

	Without Particle	30 nanometers particle	20 nanometers particle
Exp.	0.048	0.087	0.029
Sim. ($\xi = 1.7 \times 10^{-4}$)	0.0031	0.0063	0.0035
Sim. ($\xi = 2.4 \times 10^{-3}$)	0.066	0.117	0.082

calculated with data from two simulations that used ξ values of $(\pm)1.7 \times 10^{-4}$ and $(\pm)2.4 \times 10^{-3}$, **Table 2** The simulations replicate the relative sizes of the asymmetry in the absence and presence of 20 and 30-nm NPs. However, the simulations can only mimic the absolute magnitude of the asymmetry with unrealistically large ξ values (2.4×10^{-3}). We speculate that this is due to the exclusion of the dipole associated with the zwitterionic state from the simulation model. Previous work has shown that the charge states of chiral molecules strongly influence how they alter the EM environments of chiral plasmonic structures.[11] This dependency may arise because the presence of a charge molecule with a dipole moment modifies the level of capacitive coupling within the structure. Another reason for the discrepancy between simulation and experiment is that the rough morphologies of real metasurfaces are not accounted for in the simulations. This means that simulations using idealised structural models do not account for the hotspots of enhanced chiral asymmetry ("superchiral hotspots").[29]

Although the models that include NP are crude, the electric field maps, **Figure 5**a–i, derived from them may provide some insight into why 30 nm particles are more effective at enhancing sensitivity. A potential factor that would affect the relative magnitudes of asymmetries is related to the size of the gap regions the NPs make with the side walls of the shuriken cavities. The larger 30 nm NPs can adopt geometries that on average have smaller gaps and thus more intense fields than the 20 nm particles. Another parameter that may reduce the relative size of the asymmetries for the 20-nm diameter NPs is the heterogeneity in the position of the NP. This results in the particles occupying a broader range of EM environments, which could smear out the asymmetries.[17] The effects of placing NPs at different points within the arms have also been modelled (see S8, S9, and S11; Table S1, Supporting Information). These data show that altering the position of the NP within the arm has no significant effect on the magnitudes of the asymmetries. This implies that the hotspots formed between the NP and the surfaces of the arms predominantly influence the magnitude of the asymmetries. However, positioning the 20 nm nanoparticle in the same location as the 30 nm nanoparticle results in a decrease in asymmetry, from 0.082 to 0.065. This reduction is likely due to an increased separation between the nanoparticle and the shuriken cavity walls. This finding supports our hypothesis that the greater positional heterogeneity of the 20 nm nanoparticles within the cavity leads to reduced observed asymmetries.

In summary, the benchmarking experiments establish the efficacy of the approach with Raman signal asymmetries correlating with the absolute configurations of the amino acids. In addition, the introduction of 30-nm Au nanoparticles provided the greatest improvement in signal-to-noise ratio.

2.4. Random Coil and α-Helical Poly-L and D-Lysine

To exemplify the potential application of this phenomenon for monitoring biomolecular conformation, we utilized model systems L-, D-, and rac-polylysine (PL), with masses ranging from 15 to 30 kDa. The conformation of PL can be controlled via pH, with random coil and α-helical structures observed at low (pH < 7) and high (pH > 11) pH levels, respectively. In contrast to cysteine and L-glutathione, L-/D-PL lacks a free thiol group and thus does not chemisorb to the Au metafilm. PL and BPDT were co-deposited on the substrate by incubating the metafilm substrates in solutions (see methods). Adsorption of random coil or α-helical poly-L/D-lysine results in the same level of shifts within the precision of the measurement in the plasmonic resonances for LH and RH substrates (≈2 nm), indicative of the same amount of material on both LH and RH substrates [see S10, Supporting Information] and the same quantities of random coil and α-helical PL. A notable distinction between poly-L/D-lysine and the benchmarking L-/D-/LD-cysteine and L-glutathione is the amount of material detected in the experiment. Due to the peptide's larger mass, which is 100–200 times that of the simple amino acids, this means that 1.5-3 attomoles will be detected within the field of view of the Raman microscope.

Guided by the benchmarking data, Raman measurements were performed in the absence and presence of 30 nm Au NP. Individual normalized spectra and difference spectra are shown in **Figures 6**a–i and 7a–d. Shaded regions in the spectra shows the standard deviation of 15 measurements collected from three samples. Two clear observations can be made from these data. First, symmetric responses are only observed for the enantiomers of the α-helical PL, with no discernible asymmetry for the random coil. Second, the sign of the asymmetries has the same dependence on absolute configuration as the benchmarking experiments on cysteine and glutathione, an observation that further validates the phenomenon and implies a link to the optical rotatory response, and hence the Pasteur coefficient of the chiral molecules. The dependence of the effect on the level of structural order, which is high and low respectively for α-helical and random coil, is consistent with previous work on chiral sensing.[12,14–16,30]

2.5. Hotspots with Extreme Optical Chirality

In conventional ROA spectroscopy, the technique detects how Raman scattering varies with the circular polarization of incident light. Typically, this involves comparing the intensities of Raman scattering for right- and left-circularly polarized light to determine the chiral properties of molecules.[6]

In contrast, the experiment described here employs chiral nanocavities with near fields exhibiting chiral asymmetries, quantified by the optical chirality (C) parameter.[31,32] The handedness of these near fields changes when switching between enantiomorphs. Rather than altering the polarization of the incident light, we adjust the handedness of the localized fields surrounding the chiral nanostructures.

Crucially, this study does not measure the optical activity of chiral molecules directly. Instead, it probes the changes in the electromagnetic (EM) environment by observing the response of

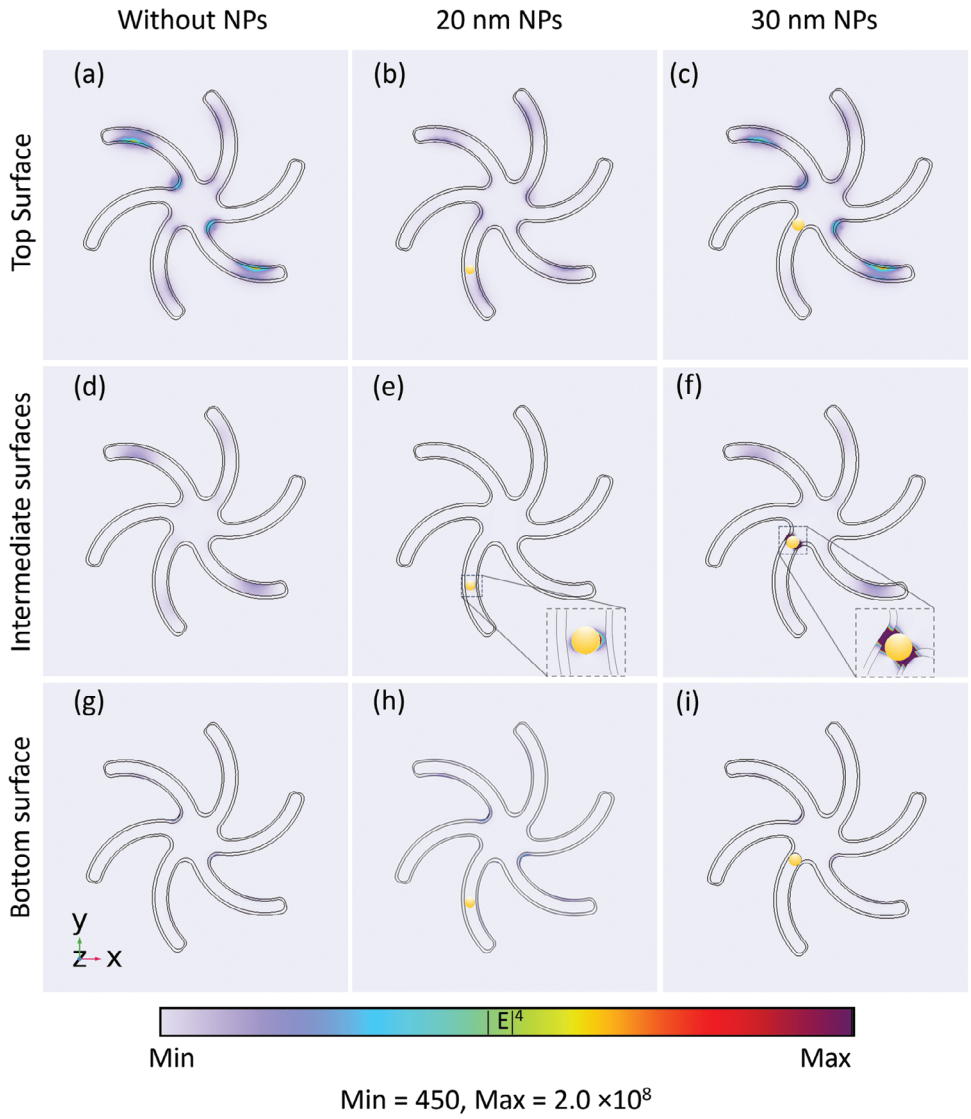

Figure 5. Maps of $|E|^4$ derived from numerical simulations at the Raman excitation wavelength for three horizontal planes (for the metasurfaces with and without NP): a–c) passing 5 nm above the top of the metasurfaces and d–f) passing 3 nm above the centre of the NPs. For no NP, 20 and 30-nm nanoparticles this plane passes either 55, 57, or 52 nm below the top surface, respectively; and g–i) passes 90 nm below the top surface. Polarisation of the incident light is along the Y axis in all cases, and the axis orientation is shown in the bottom right corner of the figure. The lateral periodicity of the simulated structure is 720 nm.

an achiral molecule. This response is influenced by the interaction between the chiral near field and a chiral molecule, allowing us to infer the EM modifications caused by the presence of chiral asymmetries. In localized regions, the near field can achieve an optical chirality exceeding that of circularly polarized light ($|C| > 1$)[3] a phenomenon known as superchirality. This enhanced chiral asymmetry can significantly amplify the dichroic responses of optically active measurements by a factor proportional to $|C|$.[33]

Numerical simulations (see **Figure 8**) map the chiral asymmetries of the near-field environment under linearly polarized light. These simulations show that in localized regions within shuriken-shaped nanocavities, the optical chirality can surpass that of circularly polarized light ($|C| > 1$). For instance, without nanoparticles, the maximum optical chirality observed is approximately $|C| \approx 33$. However, with the introduction of nanoparticles, extremely high values of optical chirality, up to $|C| \approx 6900$, are achieved in small regions between the shuriken cavity walls and the nanoparticles. This dramatic increase is termed "Extreme Optical Chirality."

Despite these highly localized hotspots of extreme optical chirality (labelled C_{max}), their impact on the overall EM environment is limited because they occupy only a small fraction of the entire near-field region. As a result, while there is a significant localized enhancement, the average effect across the entire metasurface remains modest. This is supported by surface-averaged optical chirality values (C_{avg}), which show only a minor increase from $|C_{avg}| = 0.01$ without nanoparticles to $|C_{avg}| = 0.06$ with nanoparticles across the near-field plane intersecting the nanoparticles.

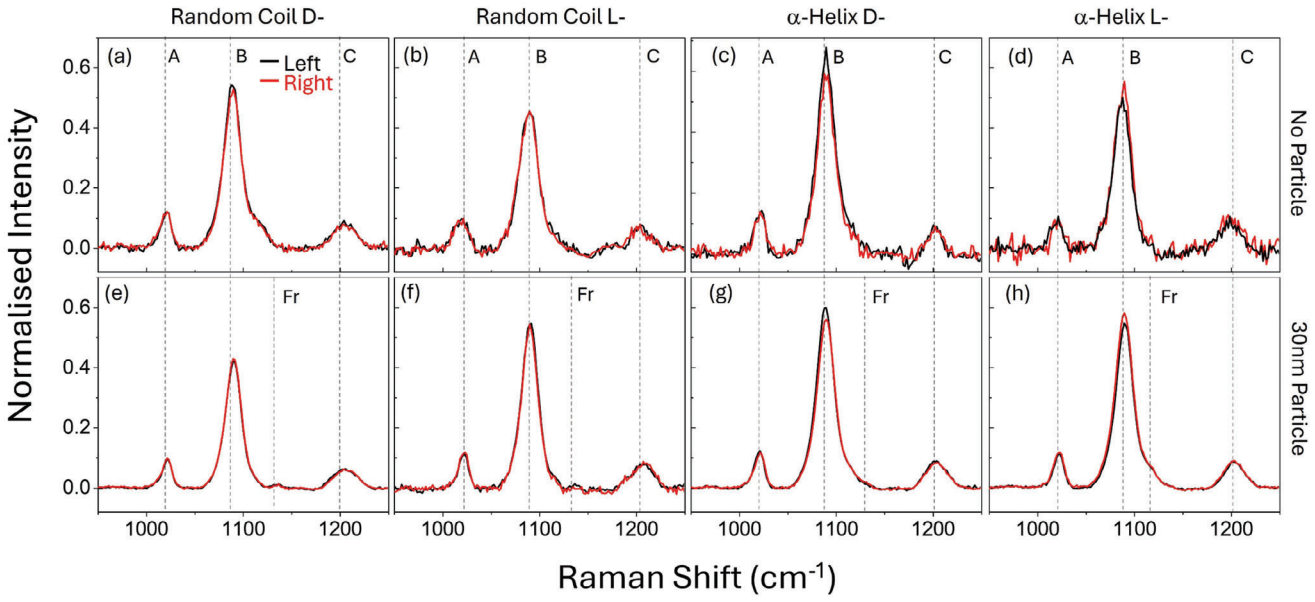

Figure 6. Raman spectra normalized at 1590 cm^{-1} collected from the left (black) and right (red) metasurfaces spanning the A, B, and C Raman peaks: a–d) BPDT + poly-L/D-lysine for random coil and α helix structure (b) with 30 nm NPs.

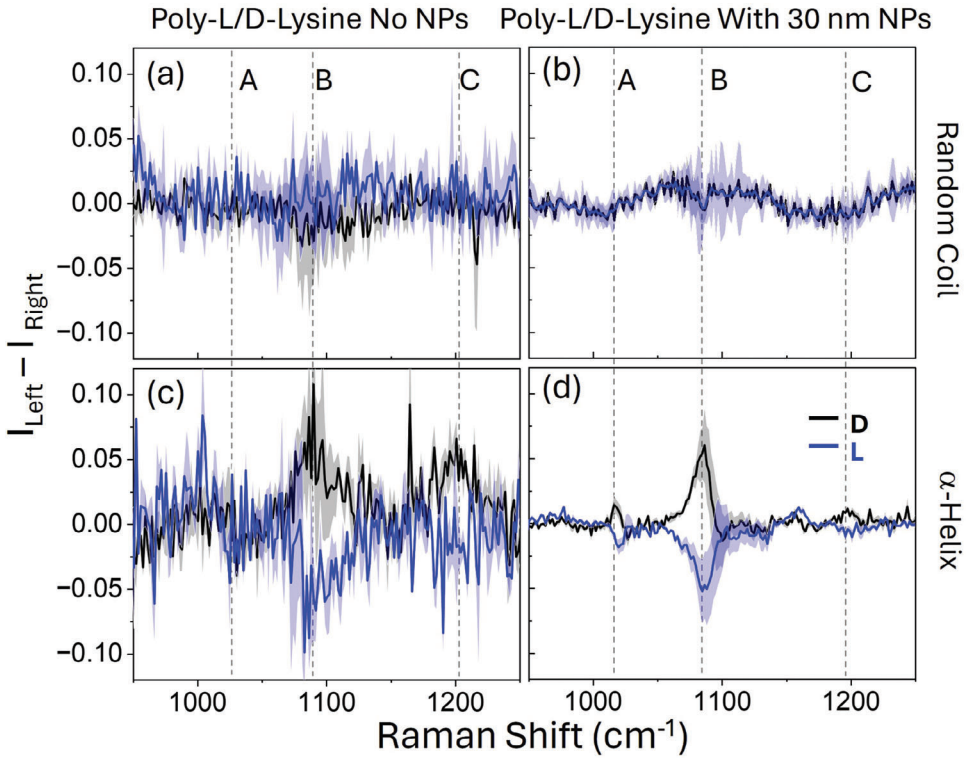

Figure 7. The difference spectra derived from the Raman intensities from left and right-handed chiral metasurfaces ($I_{left} - I_{right}$), for: a,b) BPDT + poly-L/D-lysine random coil structure without and, c,d) BPDT + poly-L/D-lysine α helix structure with 30 nm NPs. The shaded region in each spectrum represents the standard deviation derived from 15 measurements.

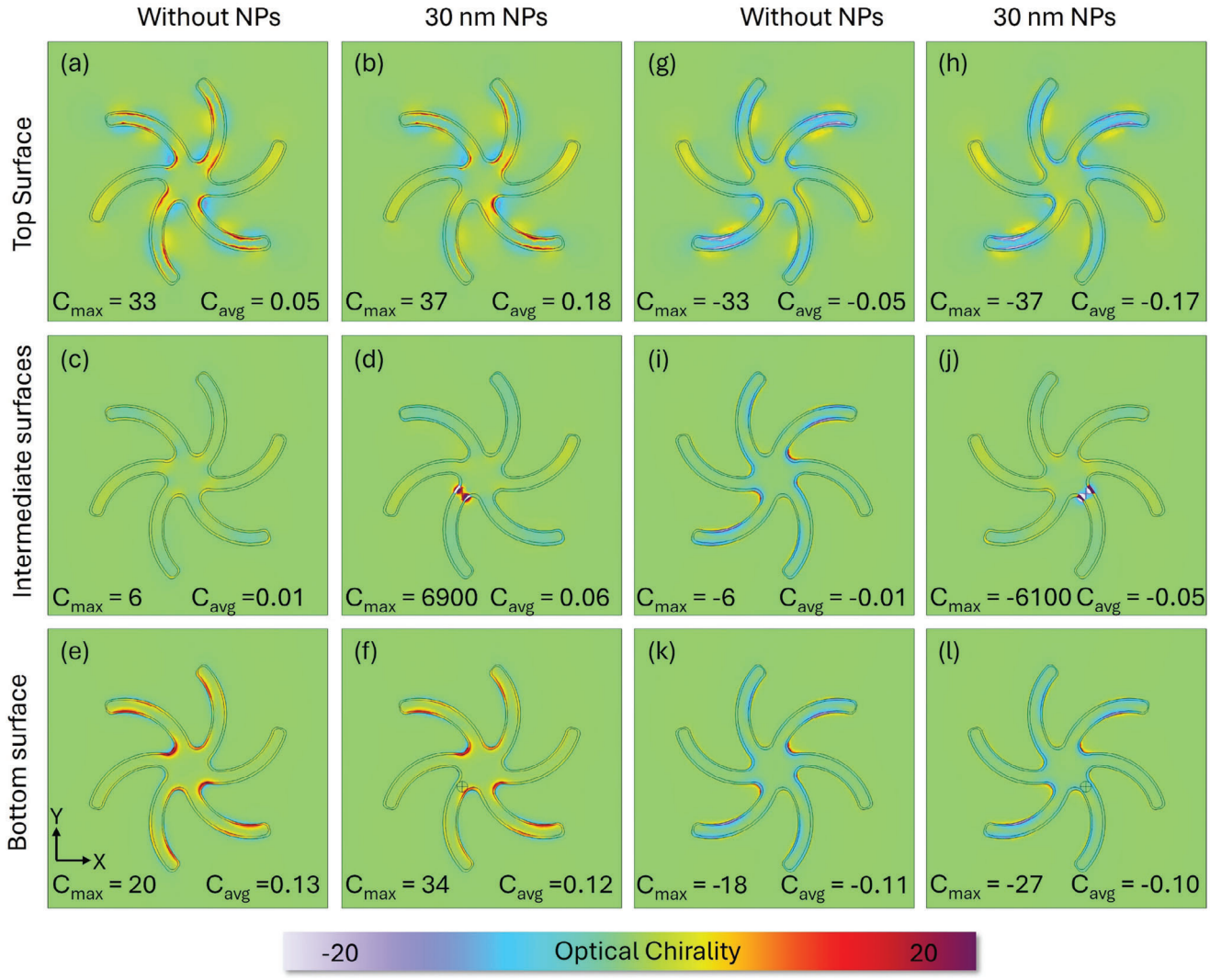

Figure 8. Maps of Optical Chirality (C) derived from numerical simulations at the Raman excitation wavelength for three horizontal planes (for the metasurfaces without NP and with NP): a–f) for LH metasurfaces and g–l) RH metasurfaces, respectively. The top surface is 5 nm above the metamaterial surface, the intermediate surface passes through the centre of NP at 55 nm, and the bottom surface is 90 nm below the top surface. The periodicity of the structure is 720 nm. C_{max} and C_{avg} represents the maximum chirality and average chirality, respectively, in the given horizontal plane.

In summary, although the introduction of nanoparticles creates regions of extreme optical chirality, their overall influence is limited. These hotspots represent only a minor portion of the near-field environment, resulting in a modest average effect across the metasurface.

3. Conclusion

This study highlights the potential of Raman reporters for investigating changes in the electromagnetic (EM) environment at the molecular level. The method offers high chiral sensitivity by detecting with great precision how the introduction of chiral molecules alters the chiral EM environment at the molecular scale within the nanocavity. The use of Raman reporters to probe chiral electromagnetic (EM) environments is highly sensitive to the presence of chiral species but relatively insensitive in distinguishing between different molecular species. However, our study specifically focuses on probing and analysing the secondary structure of biomolecules, such as α-helices and random coils, which are crucial for determining biological function and interactions. This emphasis on secondary structure sensitivity aligns with established techniques like electronic circular dichroism (ECD), which are proficient at detecting secondary stricture, but less effective at discriminating between differing component molecules. By leveraging our method's sensitivity to secondary structures, we aim to deepen our understanding of biomolecular conformational dynamics and functional states. This approach provides valuable insights that transcend the limitations of primary structure-based distinctions, enhancing our ability to elucidate the complex relationships between structure, function, and biological activity in biomolecules.

The observed phenomenon is sensitive to both the absolute configuration and the higher-order structures of (bio)molecules. This chirally sensitive Raman effect boasts a remarkable[15]

tenfold increase in sensitivity compared with the established technique of ROA. It is also 9 fold more sensitive than a previously reported ROA amplification method using a dielectric nanophotonic platform.

Although the introduction of nanoparticles does not significantly increase the level of asymmetry in the difference spectra, their presence enhances the overall signal-to-noise ratio (SNR). Consequently, for biopolymers such as poly-L/D-lysine, the improved SNR from metasurfaces with 30 nm nanoparticles suggests that a sensitivity of 100 zeptomoles is readily achievable.

Importantly, the sensitivity to biomolecular structure remains a key advantage, mirroring one of ROA's most valuable capabilities. In addition, the utilisation of low-cost, high-throughput manufactured templated metafilms makes this phenomenon ideal for developing novel technologies required for ultrasensitive biophysical measurements in life and chemical sciences.

4. Experimental Section

Fabrication of the Chiral Metasurface: The polycarbonate templates were prepared by injection moulding. A silicon substrate was cleaned and coated with 80 nm thick PMMA (polymethyl methacrylate) to perform electron beam lithography. The shuriken pattern (periodicity 720 nm, arm-to-arm length 520 nm, arm width 30 nm) was transferred using electron beam writing (Elvacite 2041, Lucite International) operating at 100 kV. After lithography, the pattern was developed by immersion in a mixture of methyl isobutyl ketone and isopropyl alcohol. This pattern was transferred on 300 µm thick nickel sim by electroplating on the Si master slide. This nickel sim is mounted on a custom-made setup attached to a fully automated injection moulding machine (Engel Victory Tech 28 tonnes) to produce a polymer slide using polycarbonate (Makrolon DP2015) as feedstock. The plastic samples were coated with Au using electron beam evaporation to form the chiral metafilm.

Sample Preparation: SAM formation on the metasurface was achieved using solution phase deposition. Briefly, shuriken metasurfaces were first sonicated in ethanol for 5 min, followed by plasma cleaning for 2 min at 100 W. A 0.5 mg ml^{-1} solution of cysteine and biphenyl-4,4′-dithiol were prepared in water and methanol, respectively, and mixed together in a 1:1 ratio if required. The metasurfaces were immersed in the appropriate solution for ≈16 h to form the required SAM. The samples were then rinsed with water and methanol, followed by drying under a nitrogen gas flow. Three types of samples were prepared: two with different cysteine enantiomers, one with the L-enantiomer, and the other with the D-enantiomer. The third sample is a racemic mixture comprising both enantiomers. Au nanoparticles with optical density 1 and a stabilized suspension in citrate buffer solution were purchased from Merck. If required, NPs were deposited onto the SAM functionalised metasurface by immersion into the NP solution, and they were rinsed after removal.

L-glutathione samples were prepared in the same manner as cysteine. The random coil structure of the poly-L/D-lysine sample was prepared in the same way as cysteine, while the α-helix structure of poly-L/D-lysine was prepared using a slightly different method. Poly-L/D-lysine was dissolved in pH 11 solution and mixed with BPDT solution. After mixing, the pH of this solution is reduced and further adjusted to pH 11. After pH adjustment, the same method is used to further prepare the solution.

Surface Characterization: SEM images of the metasurfaces were acquired using an SU8240 (Hitachi) at 10 kV.

Reflection and ORD Measurements: A home-built polarimeter setup that comprised tungsten halogen light source (Thor lab) polarisers 10x, 0.3 numerical aperture (NA) objective, and a camera. The samples were aligned with a camera, and the reflected light was routed to a spectrometer (Ocean optics USB4000). For reflection spectra, a plain Au film was used as background, which was then used for normalisation. ORD spectra were measured using the stokes method. Linearly polarized light was incident at the surface of the sample, and the reflected light was measured for four different polarisation states (0, ±45, and 90°) with respect to the incident light.

Raman Measurements: Raman measurements were performed using an NT-MDT NTEGRA Raman microscope. Samples were excited with a 20x, 0.45 NA Olympus objective with a 632.8 nm He-Ne laser with 120 µW power. 5 measurements were performed on three pairs of enantiomorphic metasurfaces (LH and RH). Each Raman spectrum was acquired for 20 s.

Numerical Simulation: Finite element method-based numerical simulations were performed using a commercial package (COMSOL V6.0 Multiphysics Software, Wave Optics module). Single shuriken models with periodic boundary conditions were used to replicate the metasurfaces. A 5-nm chiral dielectric layer was placed over the shuriken to mimic the chiral nature of the adsorbed cysteine. Perfectly matched boundary conditions were used at the input and output ports to minimise the internal reflection. The diameter of the shuriken structure was 520 nm with an arm width of 30 nm, and NPs were placed just above the chiral dielectric layer to calculate the enhancement and asymmetry average of $|E|^2$ at 632.8 and 703.5 nm in the chiral layer, and the gap outside the layer was used.

Supporting Information

Supporting Information is available from the Wiley Online Library or from the author.

Acknowledgements

A.K. would like to acknowledge support from the UKRI, EPSRC (EP/S001514/1 and EP/S029168/1) and the James Watt Nanofabrication Centre. N.G. and M.K. acknowledge support from both the EPSRC (EP/S012745/1 and EP/S029168/1) and the Leverhulme Trust (RF-2019-023). O.L. would like to acknowledge the support of GACR under the project (23–08509S).

Conflict of Interest

The authors declare no conflict of interest.

Data Availability Statement

The data that support the findings of this study are available in the supplementary material of this article.

Keywords

chirality, enantiomer, Plasmonics, SERS, super chirality optical chirality

Received: June 4, 2024
Revised: July 8, 2024
Published online:

[1] Y. Zhao, A. N. Askarpour, L. Sun, J. Shi, X. Li, A. Alu, *Nat. Commun.* **2017**, *8*, 14180.
[2] M. L. Solomon, J. M. Abendroth, L. V. Poulikakos, J. Hu, J. A. Dionne, *J. Am. Chem. Soc.* **2020**, *142*, 18304.
[3] E. Hendry, T. Carpy, J. Johnston, M. Popland, R. V. Mikhaylovskiy, A. J. Lapthorn, S. M. Kelly, L. D. Barron, N. Gadegaard, M. Kadodwala, *Nat. Nanotechnol.* **2010**, *5*, 783.

[4] T.-H. Xiao, Z. Cheng, Z. Luo, A. Isozaki, K. Hiramatsu, T. Itoh, M. Nomura, S. Iwamoto, K. Goda, *Nat. Commun.* **2021**, *12*, 3062.
[5] T. R. Leite, L. Zschiedrich, O. Kizilkaya, K. M. McPeak, *Nano Lett.* **2022**, *22*, 7343.
[6] E. W. Blanch, L. D. R. Barron, in *Emerging Raman Applications and Techniques in Biomedical and Pharmaceutical Fields* (Eds: P. Matousek, M. D. Morris), Biological and Medical Physics Biomedical Engineering, Springer, xx xx, **2010**, pp. 153, https://link.springer.com/book/10.1007/978-3-642-02649-2.
[7] L. D. Barron, *Biomed. Spectrosc. Imaging* **2015**, *4*, 223.
[8] O. Guselnikova, R. Elashnikov, V. Svorcik, M. Kartau, C. Gilroy, N. Gadegaard, M. Kadodwala, A. S. S. Karimullah, O. Lyutakov, *Nanoscale Horiz.* **2023**, *8*, 499.
[9] A. S. Karimullah, C. Jack, R. Tullius, V. M. Rotello, G. Cooke, N. Gadegaard, L. D. Barron, M. Kadodwala, *Adv. Mater.* **2015**, *27*, 5610.
[10] C. Kelly, L. Khosravi Khorashad, N. Gadegaard, L. D. Barron, A. O. Govorov, A. S. Karimullah, M. Kadodwala, *ACS Photonics* **2018**, *5*, 535.
[11] M. Rodier, C. Keijzer, J. Milner, A. S. Karimullah, A. W. Roszak, L. D. Barron, N. Gadegaard, A. J. Lapthorn, M. Kadodwala, *Nanoscale Horiz.* **2020**, *5*, 336.
[12] R. Tullius, A. S. Karimullah, M. Rodier, B. Fitzpatrick, N. Gadegaard, L. D. Barron, V. M. Rotello, G. Cooke, A. Lapthorn, M. Kadodwala, *J. Am. Chem. Soc.* **2015**, *137*, 8380.
[13] R. Tullius, G. W. Platt, L. Khosravi Khorashad, N. Gadegaard, A. J. Lapthorn, V. M. Rotello, G. Cooke, L. D. Barron, A. O. Govorov, A. S. Karimullah, M. Kadodwala, *ACS Nano* **2017**, *11*, 12049.
[14] C. Kelly, R. Tullius, A. J. Lapthorn, N. Gadegaard, G. Cooke, L. D. Barron, A. S. Karimullah, V. M. Rotello, M. Kadodwala, *J. Am. Chem. Soc.* **2018**, *140*, 8509.
[15] M. Rodier, C. Keijzer, J. Milner, A. S. Karimullah, L. D. Barron, N. Gadegaard, A. J. Lapthorn, M. Kadodwala, *J. Phys. Chem. Lett.* **2019**, *10*, 6105.
[16] T. Kakkar, C. Keijzer, M. Rodier, T. Bukharova, M. Taliansky, A. J. Love, J. J. Milner, A. S. Karimullah, L. D. Barron, N. Gadegaard, A. J. Lapthorn, M. Kadodwala, *Light: Sci. Appl.* **2020**, *9*, 195.
[17] M. Hajji, M. Cariello, C. Gilroy, M. Kartau, C. D. Syme, A. Karimullah, N. Gadegaard, A. Malfait, P. Woisel, G. Cooke, W. J. Peveler, M. Kadodwala, *ACS Nano* **2021**, *15*, 19905.
[18] V. Tabouillot, R. Kumar, P. L. Lalaguna, M. Hajji, R. Clarke, A. S. Karimullah, A. R. Thomson, A. Sutherland, N. Gadegaard, S. Hashiyada, M. Kadodwala, *ACS Photonics* **2022**, *9*, 3617.
[19] D. P. Santos, M. L. A. Temperini, A. G. Brolo, *Acc. Chem. Res.* **2019**, *52*, 456.
[20] E.-O. Ganbold, S.-W. Joo, *Bull. Korean Chem. Soc.* **2015**, *36*, 887.
[21] M. Kartau, A. Skvortsova, V. Tabouillot, S. K. Chaubey, P. Bainova, R. Kumar, V. Burtsev, V. Svorcik, N. Gadegaard, S. W. Im, M. Urbanova, O. Lyutakov, M. Kadodwala, A. S. Karimullah, *Adv. Opt. Mater.* **2023**, *11*, 2202991.
[22] G. Dodero, L. De Michieli, O. Cavalleri, R. Rolandi, L. Oliveri, A. Daccà, R. Parodi, *Colloids Surf. A* **2000**, *175*, 121.
[23] S. Fischer, A. C. Papageorgiou, M. Marschall, J. Reichert, K. Diller, F. Klappenberger, F. Allegretti, A. Nefedov, C. Wöll, J. V. Barth, A. Cysteine on, *J. Phys. Chem. C* **2012**, *116*, 20356.
[24] D. A. MacLaren, J. Johnston, D. A. Duncan, H. Marchetto, S. S. Dhesi, N. Gadegaard, M. Kadodwala, *Phys. Chem. Chem. Phys.* **2009**, *11*, 8413.
[25] N. Bovet, N. McMillan, N. Gadegaard, M. Kadodwala, *J. Phys. Chem. B* **2007**, *111*, 10005.
[26] Y. R. Lee, M. S. Kim, C. H. Kwon, *Bull. Korean Chem. Soc.* **2013**, *34*, 470.
[27] N. A. Abdulrahman, Z. Fan, T. Tonooka, S. M. Kelly, N. Gadegaard, E. Hendry, A. O. Govorov, M. Kadodwala, *Nano Lett.* **2012**, *12*, 977.
[28] C. Kelly, L. K. Khorashad, N. Gadegaard, L. D. Barron, A. O. Govorov, A. S. Karimullah, M. Kadodwala, *ACS Photonics* **2018**, *5*, 535.
[29] C. Gilroy, D. J. P. Koyroytsaltis-McQuire, N. Gadegaard, A. S. Karimullah, M. Kadodwala, *Mater. Adv.* **2022**, *3*, 346.
[30] D. J. P. Koyroytsaltis-McQuire, C. Gilroy, L. D. Barron, N. Gadegaard, A. S. Karimullah, M. Kadodwala, *Adv. Photonics Res.* **2022**, *3*, 2100155.
[31] Y. Tang, A. E. Cohen, *Phys. Rev. Lett.* **2010**, *104*, 163901.
[32] D. M. Lipkin, *J. Mathemat. Phys.* **1964**, *5*, 696.
[33] Y. Tang, A. E. Cohen, *Science* **2011**, *332*, 333.